Chapter 4

Quantum effects in Bi quantum dots

Ce n'est pas le chemin qui est difficile,
c'est le difficile qui est le chemin.

Soren Kierkegaard

4.1 Introduction

Measuring and understanding quantum effects in bismuth nanodevices is extremely challenging. At the origin of this undeniable fact are the unique, complex, and sometimes exotic physical properties of bulk bismuth, that we slightly unveiled in section 2.3.1. Due to these particular properties, bismuth holds a place of choice in the history of solid state physics. Indeed, many major transport phenomena, such as the Hall, Seebeck and Shubnikov-de Haas effect were discovered thanks to this material. Bismuth has also been the 'hobby-horse' of the PCPM lab for many years.[1] In a sense, this thesis chapter is my modest personal contribution to the continuation of this tradition. Here, we present low-temperature magnetoconductance measurements in open bismuth quantum dots. The subject would deserve much more time and attention than I could consecrate, as it was only a part of my thesis. Nevertheless, this chapter can be viewed as a prospective journey in this (for the most part) unexplored field.

[1] J. P. Michenaud and J. P. Issi initiated this 'bismuth era' in the 60's

A wealth of literature on open ballistic quantum dots demonstrates that they are model systems not only for studying electron phase coherence but also to investigate *spin* coherence processes [112, 86, 84, 55, 70]. QDs magnetotransport properties give a direct access to the characteristic times relevant to these phenomena such as the phase coherence time τ_ϕ and the spin-orbit (SO) scattering time τ_{so}. Previous works focused on QDs made from GaAs/AlGaAs heterostructures, mainly because ballistic microstructures for which the electron mean free path exceeds device dimensions can be routinely fabricated thanks to advances in molecular beam epitaxy and electron beam lithography. However, other materials can show ballistic effects, and bismuth is one of them [147]. Moreover, Bi presents very specific features with respect to semiconductor materials, as discussed in section 2.3.1: an anisotropic and nonparabolic Fermi surface, a large carrier density, a strong Dresselhaus SO coupling, and a very long mean free path due to weak electron-phonon coupling, potentially attractive for ballistic device applications. Numerous studies of transport properties of Bi thin films and wires have been published and evidenced *e.g.* localization effects [22, 116, 74], quantum size effects [74, 39] and semimetal-to-semiconductor transition [74, 79].

Here, we investigate for the first time the case of a Bi sample in the zero-dimensional (0D) configuration, of first importance for ballistic effects. Indeed, as pointed out in section 1.1.3, ballistic effects were first evidenced in Bi bulk samples. In particular, we study the low temperature magnetoconductance of our sample (section 4.4). Our observations bear clear signatures of phase coherent transport in the form of universal conductance fluctuations (section 4.5), and spin-orbit coupling in the form of a weak antilocalization peak (section 4.6). From these effects, we deduce τ_ϕ and τ_{so} in our QD and compare to data on τ_ϕ and τ_{so} obtained in Bi films.

4.2 Magnetoresistance of Bi films

Low-temperature longitudinal (R_{xx}) and transverse ($R_{xy} = V_H/I$ where V_H is the Hall voltage and I the current) resistances of 80 nm-thick Bi films grown using the two-steps method are shown as a function of the magnetic field in Fig. 4.1. The field is applied perpendicular to the film plane, *i.e.* along the trigonal axis. These measurements were obtained on samples Bi_2 and Bi_3 in the van der Pauw geometry, using a lock-in technique. Differences in the absolute R_{xx} value likely come from imperfect geometry.

R_{xx} vs B is parabolic at small B and gradually becomes linear as B

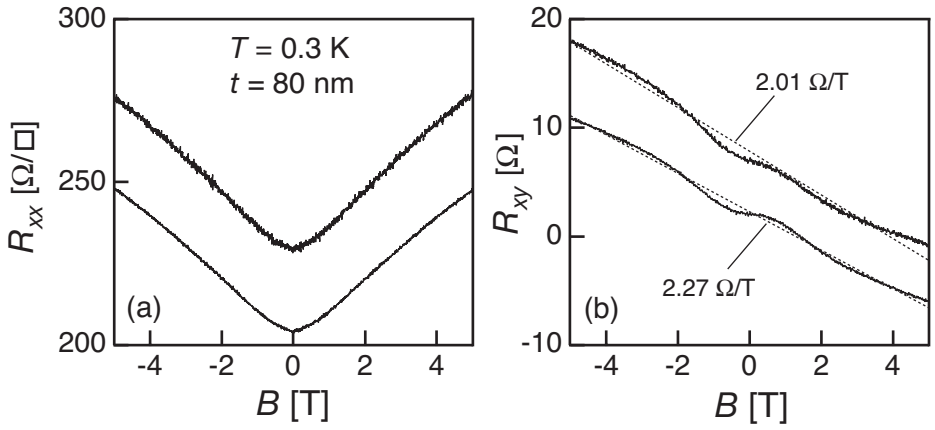

Figure 4.1: (a) Longitudinal and (b) transverse resistances vs B in two 80 nm-thick Bi film (samples Bi_2 and Bi_3), grown using the two-steps method.

increases, as previously reported in bulk Bi samples [96, 111] and Bi films measured in the same configuration [116, 39, 157]. This magnetoresistance exists in all metals and is due to the bending of the carriers' trajectories. The effect is related to $\omega_c\tau$ where ω_c is the cyclotron frequency (proportional to $1/m^*$)[2] and τ is the carrier scattering time.[3] $\omega_c\tau$ is very large in Bi, due to the small values of the effective mass tensor components and the large τ compared to other materials.[4] In section 4.6, we will give more details about the low-B dependence of the longitudinal conductance of the films.

The Hall effect is negative [negative V_H for positive B, see Fig. 4.1(b)], indicating that the electron contribution to electrical conductivity predominates over that of holes in our samples, in agreement with previous reports of Hall effect measured on Bi films of similar thickness [40]. As $R_{xy} \neq 0$ at $B = 0$ T, there is a longitudinal (R_{xx}) contribution to the curves shown in Fig. 4.1(b). It is therefore not straightforward to analyze the nonlinear contribution in this curve, as it can originate from the nonlinear contribution of R_{xx} or R_{xy} vs B (mixing effect), and may even come from the Shubnikov-de Haas effect.

[2] in the case of a material with an isotropic carrier effective mass.

[3] More intuitively, $\omega_c\tau$ corresponds to the average "turn angle" of the carriers within the scattering time τ, due to the effect of the magnetic field.

[4] As an example, Allers and Webber [7] report a spectacular increase by a factor of 24×10^6 of the resistance of a Bi single crystal at 4.2 K due to the application of a magnetic field of 10 T .

4.3 Carrier density, mobility and effective mass

In isotropic materials where *e.g.* electrons are the majority carriers, one could readily calculate the electron surface density n_s and mobility μ from R_{xx} and R_{xy} vs B, using the classical relations $n_s = \left[|e|\frac{dR_{xy}}{dB}\right]^{-1}$ and $\mu = [|e|n_s R_{xx}]^{-1}$ where e is the electron charge. In Bi, however, things are much more complicated: both electrons and holes contribute to the transport properties, and electron and hole masses and mobilities are tensors. The determination of all the tensors components in bulk materials, as well as their temperature and magnetic field dependences, requires a large amount of work, both for collecting and analyzing the data (see *e.g.* Ref. [118]). Furthermore, the carrier density and mobility are affected by dimensionality effects in Bi (see *e.g.* Ref. [127]). This means that the carrier density and mobility in thin films cannot be directly calculated from bulk values.

Fortunately, our measurement configuration limits the number of parameters to be determined: as B is oriented along the trigonal axis (perpendicular to sample surface), and as the film is relatively thin, we neglect the motion of the carriers in the direction perpendicular to the surface of our samples. In the plane of our films, the Bi crystallites have different crystal orientations. As the areas of our films are large enough (with respect to the size of the crystallites), their longitudinal and transverse resistances do not depend on the orientation of the leads, [5] and the carrier properties therefore 'look' isotropic at the macroscopic scale.

On the contrary, in the case of a single-crystal sample such as the Bi cavity (sample Bi_1), it is clear that one *should* take into account the anisotropy of the transport properties. However, to the best of our knowledge, anisotropy is not taken into account in theories presented in chapter 1, which will be used to analyze data from the Bi cavity. Anyway, we have no direct means to obtain the components of the mobility tensor in the Bi cavity. We will therefore determine an isotropic carrier mobility and effective mass from the data on films, and keep these values for the analysis of the Bi cavity data.

At first, we extract the carrier surface density from the Hall effect. In Bi, charge neutrality imposes that electron and hole densities are equal, which already suppresses one parameter. The Hall coefficient R_{Hall} (*i.e.* the linear part of R_{xy} vs B) is given, in our configuration, by the expression [71]:

$$R_{Hall} = \frac{4}{n_s e}\frac{(\mu_1\mu_2 - \nu_1^2)}{(\mu_1 + \mu_2 + 2\nu_1)^2}, \tag{4.1}$$

[5] This is confirmed by the similarity of R_{xx} and R_{xy} in our two films.

where ν_1 is the hole mobility in the plane of the film and μ_1 and μ_2 are the 'partial mobilities' of electrons along the principal crystal axes in the plane of the film (binary and bisectrix).

In order to limit the number of adjustable parameters, we work on the assumption that the ratios μ_1/μ_2 and μ_1/ν_1 are similar to the bulk values. For the ratio μ_1/ν_1, data from Michenaud and Issi [117] and from Hartman [71] yield a value of 5.3, with a relatively low standard deviation (10%) over the temperature range 4.2 K - 300 K. μ_1/ν_1, however has a larger standard deviation over that range (about 30%). In the temperature range of our measurements (*i.e.* below $\sim$ 9 K), bulk data yield $\mu_1/\nu_1 \sim 37$, with a much more reasonable standard deviation of $\sim$ 10%. Using these data together with R_{Hall} obtained by linear fit to R_{xy} vs B [Fig. 4.1(b)], we can solve Eq. (4.1) and we obtain $n_s = 5.5 \times 10^{16}\ m^{-2}$. This is comparable to $n_s = 8 \times 10^{16}\mathrm{m}^{-2}$ found by Partin and coworkers [127] in *single crystal* 100 nm-thick films grown on BaF_2 substrate at 20 K.

Next, we can estimate the carriers mobility from the resistance at $B = 0$ T, using the following expression [71]:

$$R_{xx}(B=0) = \frac{2}{n_s e}\frac{1}{(\mu_1 + \mu_2 + 2\nu_1)}. \tag{4.2}$$

Using the values given above for the ratios μ_1/ν_1 and μ_1/μ_2 and for n_s, we find $\mu_1 \sim 0.9$ m^2/Vs. This is almost exactly one order of magnitude smaller than the mobility found by Partin and coworkers in a 100 nm-thick single crystalline Bi film (using similar assumptions). We attribute this difference to the fact that electrons are predominantly scattered as they cross grain boundaries. This is supported by the value of the electron elastic mean free path $l_\mu \sim 340$ nm (calculated from μ_1), very close to the average crystallite radius (see Fig. 2.13(c)). We will therefore assume that electron transport is ballistic inside individual crystals in our films, as well as in sample Bi_1. Furthermore, we will also assume in the following sections that holes play a negligible role, due to their lower mobility and larger effective mass.

The last parameter that we must determine is the 'isotropic' effective mass in the plane of the films. We will work on the basis of the bulk trigonal cyclotron effective mass m_{cb} ($m_{cb} = \sqrt{m_1 m_2}$).[6] At the bottom of the conduction band, $m_{cb} = 0.018 * m_0$. Therefore, at the Fermi level in bulk Bi, the effective mass increases to $m_{cF} = 0.09 * m_0$ (according to Eq. 2.7). Due to the increase of the carrier density in films with respect

[6] Choosing a bulk value in the case of a film is justified since the effective mass tensor do not significantly vary with film thickness t, at least for $t \gtrsim 50nm$ (this was shown by Chu and coworkers [40] in the range $80 \lesssim t \lesssim 300$nm).

to bulk material,[7] the Fermi energy is larger,[8] so that the effective mass is slightly increased. In the following, we will therefore use $m^* = 0.1 * m_0$.[9]

This isotropic assumption for m^* may seem a very rough approximation, given the difference between the components m_1 and m_2 of the effective mass tensor (cf. section 2.3.1). However, we will see at the end of this chapter that it can be justified within the framework of our data analysis.

4.4 Magnetoconductance of the Bi nanocavity

Figure 4.2 shows the magnetoconductance G vs B of sample Bi_1 at different temperatures. A strong background dominates the magnetoconductance. Its lineshape is comparable to that observed on bismuth films (samples Bi_2 and Bi_3, see previous section) : a quadratic B-dependence at weak field with a lower dependence at higher fields. UCFs superimpose on this background at the lowest temperatures. They persist and are symmetric with respect to $B = 0$ up to the highest investigated magnetic field (5 T). They will be analyzed in the next section. On Figure 4.2, all curves up to 2.9 K also show a narrow conductance peak centered at $B = 0$ which we attribute to weak antilocalization (WAL). Fitting to the WAL theory and comparison with WAL data from Bi films is performed in section 4.6.

In addition to UCFs, broader features are also visible in G vs B. This second type of fluctuations is clearly evidenced in Fig. 4.3, showing $\delta G = G[T] - G[T = 9.6K]$ vs B. Their characteristic magnetic field is similar to that of the fluctuations associated to classical orbits in InGaAs QDs (section 3.3).

Assuming that the classical cyclotron radius formula [Eq. (1.3)] is still valid for our Bi device, we calculated the magnetic field corresponding to some possible electron trajectories shown above Fig. 4.3. The correspondance between maxima and minima in G vs B and these positions is much less clear than in the case of the InGaAs sample B_1: the position of trajectories no. 1 and 2 are somewhat shifted towards higher B with respect to the observed minimum and maximum in G vs B; moreover, no clear maximum is observed at the magnetic field corresponding to trajectory no. 3.

Several causes may explain these discrepancies. At first, the sheet electron density may be slightly different from $5.5 \times 10^{16} \mathrm{m}^{-2}$, either because

[7] The volume density corresponding to $n_s = 5.5 \times 10^{16}$ m^{-2} is $n = 6.9 \times 10^{23}$ m^{-3}. Measurements in bulk Bi yield $n = 2.75 \times 10^{23}$ m^{-3} [139] (see also Ref. [127]).

[8] Indeed, in rough approximation, $E_F \propto n^{2/3}$ [88]

[9] Such a value of $m^* = 0.1 * m_0$ for electrons in thin films is commonly used in the litterature; see *e.g.* Ref. [116] (a hole mass of $1 * m_0$ is also assumed in this reference).

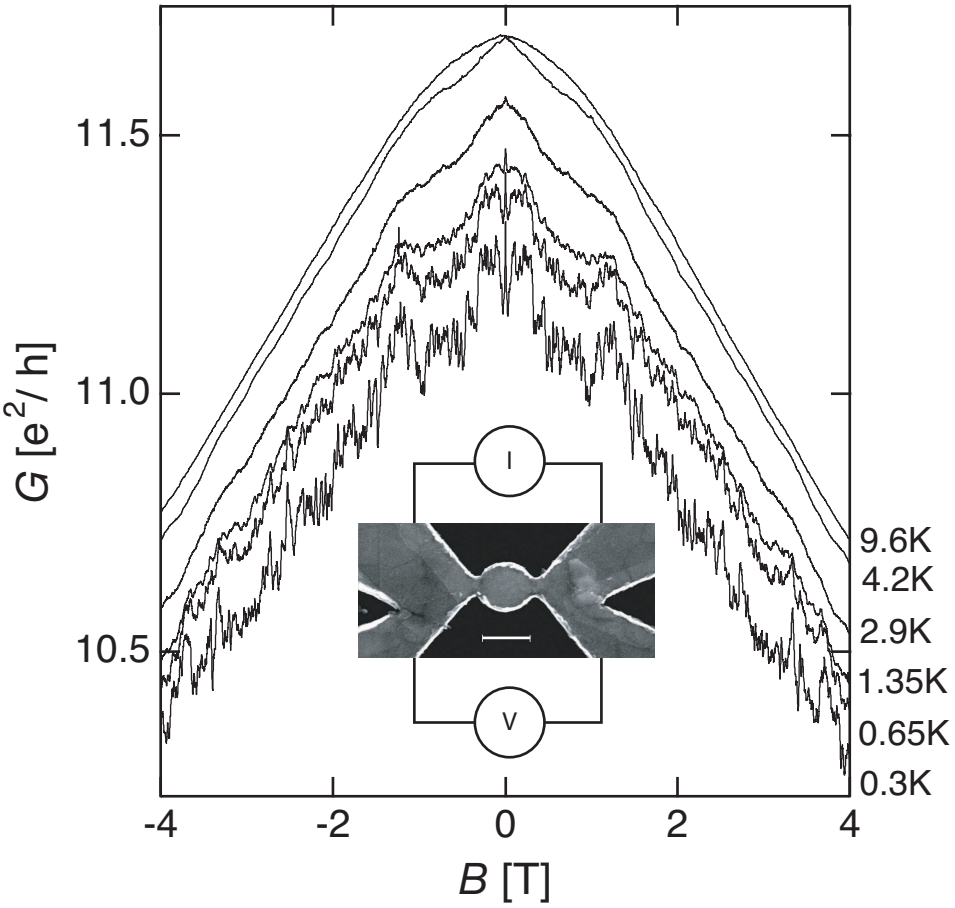

Figure 4.2: T-dependence of the magnetoconductance of Bi_1. The inset shows an electron micrograph of the cavity and the measurement setup. The white bar represents 500 nm.

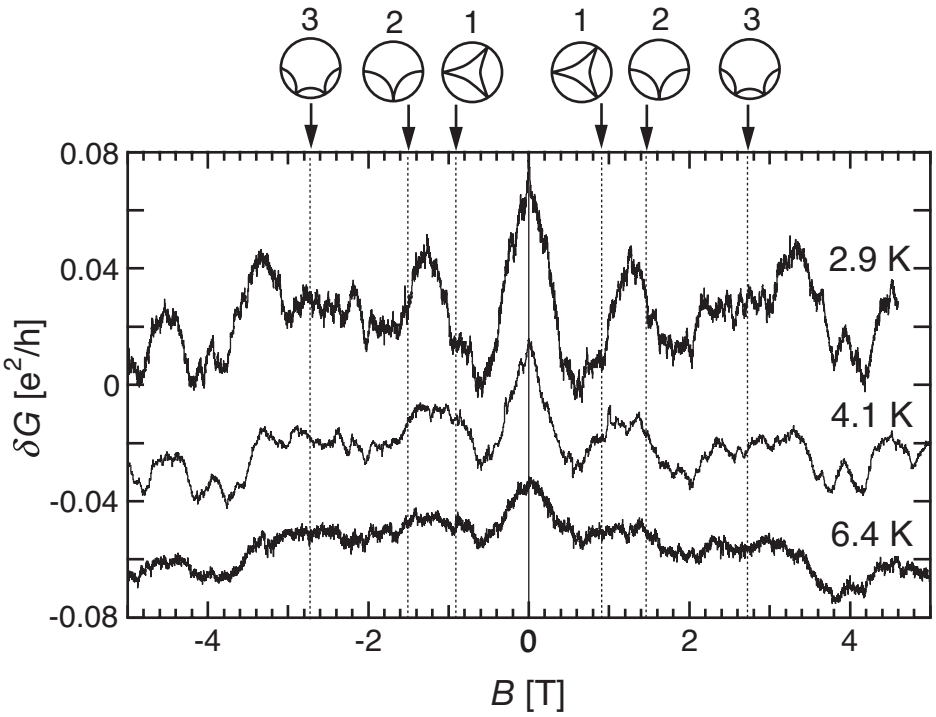

Figure 4.3: δG vs B in Bi_1 at indicated temperatures, with the position of some possible electron trajectories inside the cavity

our estimation is too rough, or because the density in the QD is effectively reduced with respect to the film value due to the lateral confinement. Secondly, Eq. (1.3) is correct only if $k_F = \sqrt{2\pi n_s}$, *i.e.*, only in a strictly two-dimensional sample, which is probably abusive in our case. Moreover, Shubnikov-de Haas oscillations may be visible in the QD sample (especially at high-B), and could interfere with the maxima and minima associated with classical orbits.[10] We have also neglected up to here the contributions of holes: the possible mixing of electron and hole focusing in our cavity is another cause of increased complexity. Finally, the electron trajectories in real space are more complicated than the simple circular motion assumed here. They should be determined based on the fact that electrons move along or-

[10] A complicated pattern of Shubnikov-de Haas oscillations has been observed in Bi thin films by several authors (see e.g. Refs. [127, 157]). As most physical phenomena observed in Bi, the oscillations depend on the crystal orientation, which is not known in our cavity.

bits of constant energy on the Fermi surface (in the reciprocal space), which are elliptic in Bi. The conjunction of all these causes impedes a complete understanding of the origin of these oscillations in the background magnetoconductance.

4.5 UCFs analysis

In this section we use different RMT-based models to find the phase coherence time τ_ϕ from UCFs data in Bi_1. Basically, τ_ϕ can be obtained in Bi_1 using the same method as for InGaAs QDs (section 3.4.1). We will use Eq. (3.1) linking τ_ϕ to $var(G)$, the variance of UCFs [57].

In order to apply Eq. (3.1) to our data, we have to separate UCFs from the background magnetoconductance. The method to achieve the separation is shown on Fig. 4.4, and is identical to that used in InGaAs QDs. As the background does not obey a simple polynomial form that we could easily substract, we apply a high-pass filter to the magnetoconductance traces, with a cut-off frequency $f_c = 3\mathrm{T}^{-1}$. f_c is determined on the basis of the temperature dependence of the Fourier spectrum of $G(B)$, as illustrated in Fig. 4.4(b):[11] below f_c, the Fourier spectrum is temperature-independent, and strongly depends on T above f_c. The 'filtered' curves δG vs B are shown in Fig. 4.4(c) at 0.3 K and 4.0 K. We observe that the amplitude of the fluctuations is approximately constant over the range $0\mathrm{T} < \mathrm{B} < 4\mathrm{T}$. $var(G)$ vs T extracted after filtering $G(B)$ clearly follows a T^{-2} law over one order of magnitude in temperature [Fig. 4.4(d)].

The next step is to fit our 'filtered' variance data with a numerical evaluation of Eq. (3.1) in order to find the corresponding values of $\tau_\phi(\mathrm{dot})$. At first, we use Eq. (3.2), *i.e.* the same conductance correlator as that used for InGaAs QDs in chapter 3, which does not take spin-orbit coupling into account. As $var(G)$ is reduced by a factor of 2 in the regime of strong SO coupling [110, 55, 70], we incorporate this factor into Eq. (3.1). We have also assumed $N_1 = N_2 = 11$, where N_i is the number of mode in each QPC.[12] Filled triangles in Fig. 4.5 correspond to τ_ϕ vs T obtained with our $var(G)$ data and a numerical evaluation of Eq. (3.1). τ_ϕ follows $\tau_\phi(\mathrm{dot}) = 2.65 \times 10^{-13} T^{-1}[\mathrm{s}]$ up to $\sim$ 3K, very small compared to values obtained in GaAs and InGaAs QDs (see chapter 3 and Ref. [86, 84]).

[11] Spectra in Fig. 4.4(b) are averages of 3 fast Fourier transforms power spectra from half overlapping blocks in the range $0.3\mathrm{T} < B < 4\mathrm{T}$.

[12] Again, we use Eq. (1.14), relating the average conductance and the total number of modes. Note that assuming $N_i = 20$ changes the result by less than 1 %, since $N \ll N_\phi$

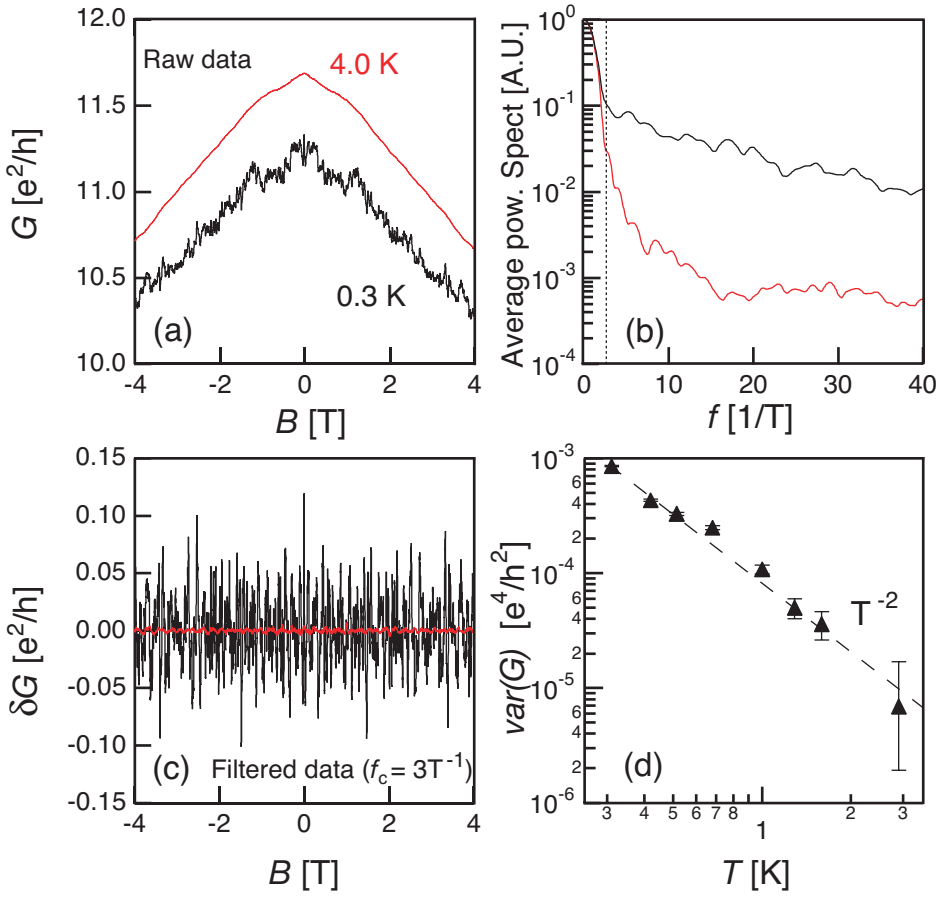

Figure 4.4: (a) G vs B in Bi_1 at 0.3 K and 4.0 K. (b) Average power spectrum as a function of the frequency $f = 1/\Delta B$ (in T^{-1}) at 4.0 K (red curve) and 0.3 K (black curve). (c) 'filtered' conductance δG vs B at 4.0 K (red curve) and 0.3 K (black curve). The cut-off frequency is 3 T^{-1}. (d) Temperature dependence of $var(G)$. The dashed line is a fit to T^{-2}.

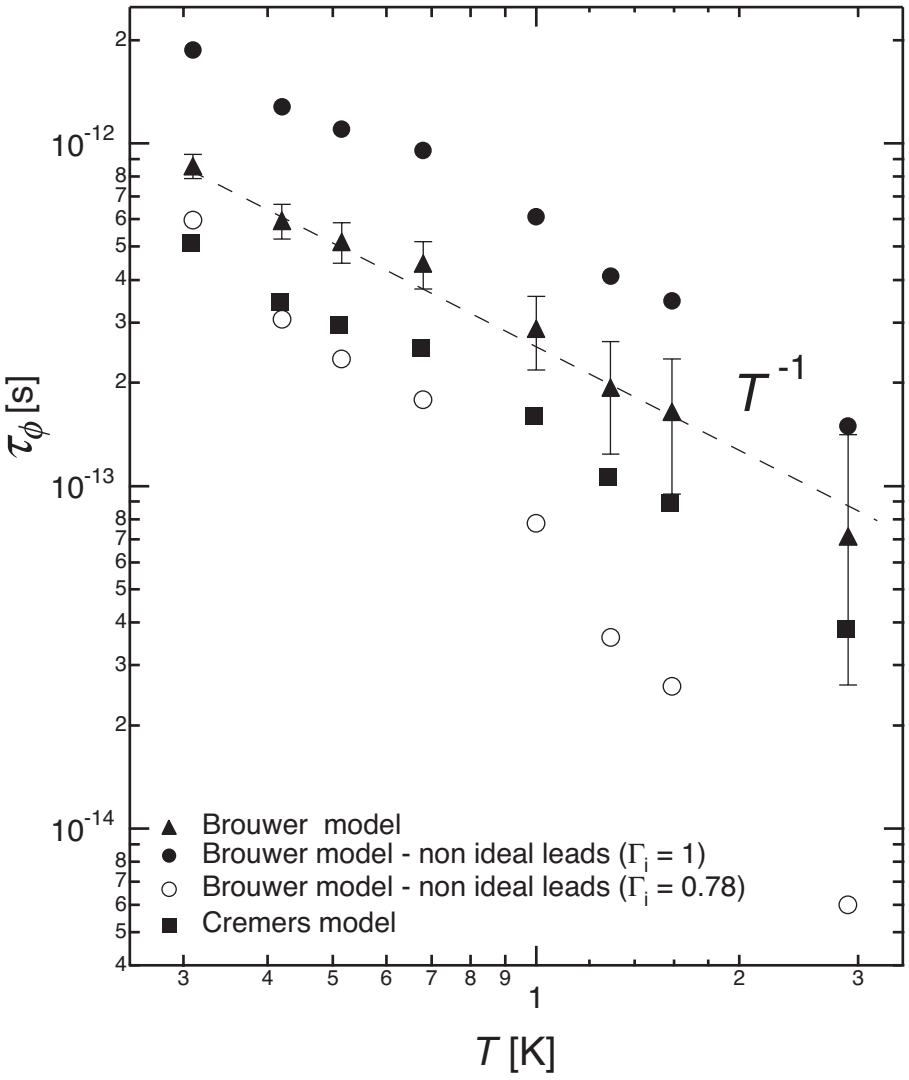

Figure 4.5: Temperature dependence of τ_ϕ in Bi_1. Triangles : τ_ϕ extracted using Eq. (3.1) and (3.2); open and filled circles: τ_ϕ extracted using Eq. (4.4) with $\Gamma_i = 0.78$ and $\Gamma_i = 1$, respectively; squares : τ_ϕ extracted using Eq. (3.1) and (4.3).

Recent theoretical works by Cremers and coworkers lead to an extension of RMT, including the effect of spin-orbit coupling and of a magnetic field applied in the plane of the heterostructure [42].[13] The generalized expression of the conductance correlator becomes:

$$cov[E, E', B, B'] = \left(\frac{e^2}{h}\right)^2 \left(\frac{N_1 N_2}{N_1 + N_2}\right)^2 (V_D + V_C), \qquad (4.3)$$

where E, E' are energies, and B, B' are two different magnetic fields. The parameters V_D and V_C have extremely cumbersome expressions. Instead of reproducing them, we refer to Ref. [42] (Eq. (30) and (31)), and we will briefly comment on our assumptions for the values of the main parameters on which they depend.

At first, we assume an isotropic spin orbit scattering length L_{SO} (λ in Ref. [42]) in the plane of the film, given by $L_{SO} = 181$nm, as determined from the Weak Antilocalization effect (see the next section). This means $L_{SO}^2 = \lambda_1 \lambda_2$ and $(\lambda_1/\lambda_2)^2 = \nu_{so} = 1$, (in the notations of Ref. [42]).[14] One of the hypothesis of the model is $L_{SO} > L$, where L is the size of the cavity. This inequality is not satisfied in our case; nevertheless, Zumbuhl and coworkers [158] could obtain a good agreement between this theory and their data, even though $L_{SO} < L$ in their samples (GaAs QDs). Some additional parameters (κ, κ' and κ'') are related to the geometry of the cavity. In the case of a circular quantum dot, with an isotropic spin-orbit coupling in the plane of the QD, one has $\kappa = 2$, $\kappa' = 1/3$ and $\kappa'' = 0.292$ [42].

Analyzing our data with Eq. (3.1) and (4.3), we obtain a second estimation of τ_ϕ vs T, shown on Fig. 4.5 (squares). We observe a very good correspondance with the previous estimation, given the number of assumptions that we had to work on. The temperature dependence, in particular, is the same, while the absolute value is slightly lower within the new RMT model.

Eq. (3.1) with the correlator given by Eq. (3.2) or (4.3) is valid for ideal point contacts. However, the grain boundaries in the openings of the cavity may contribute to some reflection in the transverse modes. Such reflection can be taken into account within the Random Matrix Theory by defining a transmission probability Γ_i for each mode i ($i = 1, \ldots, N_1$ corresponding to the first QPC, and $i = N_1 + 1, \ldots, N_1 + N_2$ corresponding to the second QPC). In that case, $var(G)$ and τ_ϕ are related by the expression [26, 27]:

[13] This theory was published shortly after the publication of our data and analysis in Phys. Rev. B [69].

[14] Additional measurements with a magnetic field in the plane of the film would indeed be necessary to determine experimentally the asymmetry parameter ν_{so}.

$$var(G) = \frac{4g_1^2 g_1'^2}{\beta g^2(g+\gamma_\phi)^2} + \frac{4(g_1^4 g_2' - g_1^4 g_3' + g_2 g_1'^4 - g_3 g_1'^4)}{\beta g^4(g+\gamma_\phi)} + \frac{6(g_1^2 g_2' + g_2 g_1'^2)^2}{\beta g^4(g+\gamma_\phi)^2} - \frac{8 g_1 g_1'(g_2 g_1'^2 + g_2' g_1^2)}{\beta g^3(g+\gamma_\phi)^2}, \quad (4.4)$$

$$g_p = \sum_{i=1}^{N_1} \Gamma_i^p, g_p' = \sum_{i=1+N_1}^{N_1+N_2} \Gamma_i^p, g = g_1 + g_1' \quad (4.5)$$

where $\gamma_\phi = 2\pi\hbar/\tau_\phi\Delta$ is the dephasing rate, and $\beta = 2$ (1) in the presence (absence) of a symmetry breaking magnetic field. Fig. 4.5 compares τ_ϕ vs T calculated using our data and Eq. (4.4) with ideal point contacts, *i.e.* $N_{1,2} = 11$ and $\Gamma_i = 1$ (for all the modes), and non-ideal point contacts *i.e.* $N_{1,2} = 14$ and $\Gamma_i = 0.78$ (for all the modes). Note that, for ideal point contacts, the result is slightly different from our previous result, because Eq.(4.4) does not include thermal smearing, contrary to Eq. (3.1) used in our analysis. We point out that, in the case of the non-ideal point contacts model, one clearly observes that τ_ϕ vs T is smaller and has a different temperature dependence (whatever the value of Γ_i). This result will be discussed later in light of values obtained for 2D films.

Overall, we observe only small differences between the results obtained with the different methods. In the following, we base our analysis on τ_ϕ vs T data obtained using the first method.

4.6 Weak antilocalization

The conductance maximum around $B = 0$ can bring independent information on both τ_ϕ and τ_{so}. The temperature dependence of the conductance G vs T at various magnetic fields is one of the tools to find out whether this central peak is indeed related to the 2D WAL effect. In 2D, when SO scattering dominates, the antilocalization induces a logarithmic correction to the zero-field conductance : $\Delta G(T) = a\ \ln(\mathrm{c} * \mathrm{T})$, where a and c are constants [22]. We find that this relation fits very well to the *raw* conductance of our nano-cavity at $B = 0$ (Fig. 4.6). Applying a small magnetic field destroys the WAL effect and leads to a negative magnetoconductance. Fig. 4.6 shows that a is changed when $|B| > 0$ but ΔG still exhibits a logarithmic temperature dependence. This is explained by disorder-induced electron-electron (e-e) interactions in 2D that add another $\ln(\mathrm{T})$ term to ΔG, which is not affected by a moderate magnetic field [22]. This picture is consistent with

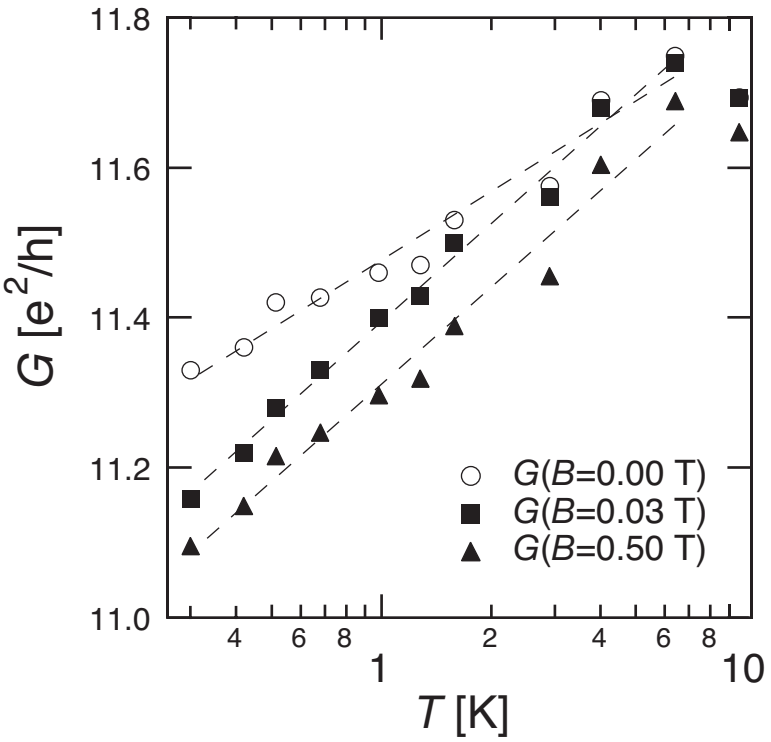

Figure 4.6: Temperature dependence of the conductance of the cavity for fixed B. Dashed lines are fits to logarithmic expressions (see text).

data in Fig. 4.6 and our nano-cavity behaves like a 2D film as far as WAL, SO and e-e interaction effects are concerned.

In order to further support this point, we report the low-B change in magnetoconductance of Bi films $\Delta G_{\Box}(T,B) = G_{\Box}(T,B) - G_{\Box}(T,B=0)$ in Fig. 4.7, and compare it to that of the Bi nano-cavity. For the dot, we assume $\Delta G_{\Box}(T,B) = \Delta G(T,B)$, which is supported by the analysis given below. We fit $\Delta G_{\Box}(T,B)$ with the expression for the WAL correction to the conductivity in 2D disordered systems [77] (in units of e^2/h):

$$\Delta G_{\Box}(T,B) = \frac{1}{2\pi}\left[\frac{3}{2}\Psi\left(\frac{1}{2}+\frac{H_2}{B}\right) - \frac{1}{2}\Psi\left(\frac{1}{2}+\frac{H_3}{B}\right) - \Psi\left(\frac{1}{2}+\frac{H_1}{B}\right)\right], \quad (4.6)$$

where Ψ is the digamma function, $H_1 = H_0 + H_{so}$, $H_2 = H_\phi(T) + \frac{4}{3}H_{so}$ and $H_3 = H_\phi(T) = aT^b$.[15] In these expressions, a and b are constants, $H_{0,\phi,so} = \hbar/(4eD\tau_{0,\phi,so})$, D is the diffusion constant and τ_0 is the elastic scattering time. We set $H_0 = 10$mT in the nanocavity and in the film.[16] The good agreement between the fit with Eq. (4.6) and our data further confirms that our samples are 2D with respect to the WAL effect.

The values obtained from this three-parameter fit are given in table 4.1, along with the phase coherence time in the dot calculated from Eq. (3.1), which is consistent with the results of the WAL analysis.[17] The phase coherence and SO scattering length are defined as $L_{\phi,so} = (\hbar/4eH_{\phi,so})^{1/2}$. τ_ϕ in the film is calculated from $\tau_\phi(\text{film}) = L_\phi(\text{film})^2/D(\text{film})$ with $D(\text{film}) = 0.05\text{m}^2/\text{s}$.[18]. Using the known values of $\tau_\phi(\text{dot})$ and $L_\phi(\text{dot})$ we can estimate $D(\text{dot}) = 0.23\text{m}^2/\text{s}$ and therefore calculate $\tau_{so}(\text{dot})$. The physical meaning of $D(\text{dot})$ is not straightforward since our nano-cavity is not in the diffusive but rather in the quasi-ballistic regime and this makes a comparison with $D(\text{film})$ difficult.

Several important conclusions can be drawn from the values gathered in table 4.1. τ_{so} is similar in both systems, consistent with a strong SO coupling in Bi resulting in a SO coupling length L_{so} smaller than device

[15] There is an error of sign in the prefactor of this expression reproduced in Ref. [69].

[16] This is equivalent to a scattering length $L_0 = (D\tau_0)^{1/2}$ of 125 nm. L_0 is more affected by small angle scattering than the mean free path l_μ. The exact value of H_0 has a weak influence : a 50% change of H_0 induces a change of $\sim 5\%$ for a and b, and $\sim 15\%$ for H_{so}.

[17] The number of squares influences the temperature dependence of $H_{\phi,dot}$: assuming *e.g.* that the dot is composed of three squares instead of one, we get $H_{\phi,dot} \propto T^2$, in contradiction with UCFs analysis.

[18] $D = 2E_F\mu/ed$, where d is the dimensionality. One assumes $E_{F,film} = E_{F,bulk} * (N_{film}/N_{bulk})^{2/3} = 50.6$meV where N_{film} and N_{bulk} are the electron volume density in Bi film and bulk respectively [88].

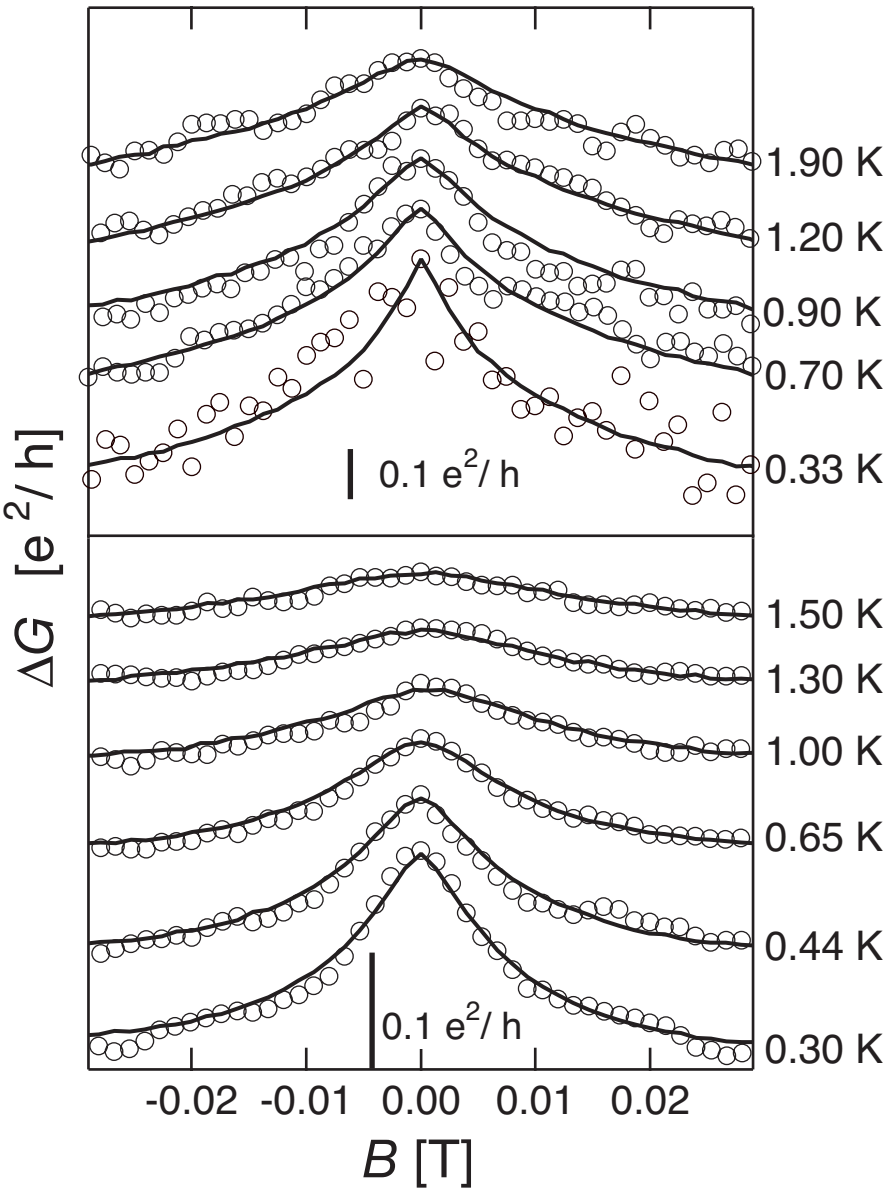

Figure 4.7: *top* : $\Delta G_{\square}(B)$ at low B for a Bi film at indicated temperatures (curves are offset for clarity). The zero-field conductance at 0.3 K is $G_{\square}(B = 0) = 113.35e^2/h$. Plain lines are fits to Eq. (4.6). *bottom* : $\Delta G_{\square}(B)$ for the dot. Plain lines are fits to Eq. (4.6).

Table 4.1: Summary of the parameters extracted from fits to WAL peaks with Eq. (4.6) and from UCFs variance analysis - *i.e.* only the coherence time in the cavity (D in the cavity is obtained by comparing the results of UCFs and WAL data analysis).

	cavity	film
H_0 (mT)	10	10
H_ϕ (mT)	$2.7(\pm 0.3) * T^{1(\pm 0.1)}$	$0.7(\pm 0.1) * T^{0.8(\pm 0.2)}$
H_{so} (mT)	$5(\pm 0.5)$	$17(\pm 4)$
L_0 (nm)	125	125
L_ϕ (nm)	$247 * T^{-1/2}$	$485 * T^{-0.4}$
L_{so} (nm)	181	98.5
τ_0 (10^{-13} s)	0.7	3.12
τ_ϕ (10^{-13} s)	$2.65 * T^{-1}$	$47 * T^{-0.8}$
τ_{so} (10^{-13} s)	1.4	1.84
D (m^2/s)	0.23	0.05

dimensions. The similarity of τ_{so} in both samples also validates the hypothesis $m^* = 0.1 m_0$. At the lowest measurement temperature, L_ϕ(dot) becomes close to the device size, so the dimensionality of the sample for phase coherent processes changes from 2D to 0D. As far as we know, the regime of weak antilocalization with L_ϕ(dot) similar to the device size has never been investigated neither experimentally nor theoretically.

Our most striking observation is the difference of more than one order of magnitude between τ_ϕ(film) and τ_ϕ(dot). A quantitative explanation may have to consider the extreme sensitivity of n_s to device dimensions in Bi [74, 79, 127], as n_s has a strong influence on e-e interactions which dominate dephasing in our temperature range. The screening length is another important factor which may be affected by confinement (although this has never been observed). Furthermore, we notice an almost similar temperature dependence of τ_ϕ in 2D and 0D samples ($\tau_\phi \propto T^{-1}$), qualitatively consistent with low energy transfer 2D e-e interactions being the dominant phase breaking process [86, 8]. However, we find a large quantitative difference between our data and the model for 2D e-e scattering: using the

expression $\tau_\phi^{-1} = \frac{k_B T}{2\pi\hbar}\frac{l_F}{l_\mu}\ln(\frac{\pi l_\mu}{l_F})$ [86, 8] where l_F is the Fermi wavelength, we obtain $\tau_\phi \sim 4\times10^{-10}T^{-1}$[s]. This is respectively 2 and 3 orders of magnitude larger than our data for the film and the dot.

4.7 Summary

In summary, we discuss low-temperature magnetoconductance data from a quasi-0D sample made from bismuth, and from Bi films. We first extract the density and mobility of electrons from longitudinal and transverse magnetoresistance from Bi films, and conclude that transport is quasi-ballistic inside crystallites forming the films. We then analyze the UCFs and WAL phenomena measured in the magnetoconductance of a single crystal Bi cavity, in order to obtain the phase coherence and spin-orbit scattering times τ_ϕ and τ_{so}. Importantly results of UCFs and WAL analysis are in good agreement, even though we use theories relying on different basis to analyze both phenomena. We evidence an anomalous reduction of the coherence time in the Bi 0D cavity with respect to 2D Bi films while we find a similar spin-orbit coupling time in both systems. The temperature dependence of τ_ϕ is consistent with dephasing by 2D electron-electron interactions in the 2D and 0D systems. However, the experimental data for τ_ϕ are much smaller than one would expect from the conventional Nyquist theory.